Single-vessel transcriptome map pathological landscapes and reveal NR2F2-mediated smooth muscle cell phenotype acquisition in capillary malformations

Vi Nguyen[1,*], Irving Mao[2,3,*], Siwuxie He[1], Isabella Castellanos[1], Mackenzie Azuero[1], Marcelo L Hochman[4,5], Yin Rong[1], Laena Pernomian[1], Elliott H Chen[6,7], Harold I Friedman[6,7], Yan-Hua Chen[8], Qun Lu[8], Daping Fan[1,9], Camilla F Wenceslau[1,9], Dong-bao Chen[10], J Stuart Nelson[11], Anil G. Jegga[2,12], Yunguan Wang[2,3,12], and Wenbin Tan[1,9]

[1]Department of Cell Biology and Anatomy, School of Medicine, University of South Carolina, Columbia, South Carolina 29209, USA

[2]Department of Pediatrics, University of Cincinnati College of Medicine, Cincinnati, Ohio 45229, USA

[3]Division of Pediatric Gastroenterology, Hepatology and Nutrition, Cincinnati Children Hospital Medical Center, Cincinnati, Ohio 45229, USA

[4]The Facial Surgery Center and the Hemangioma & Malformation Treatment Center, Charleston, South Carolina 29425, USA

[5]Department of Otolaryngology - Head and Neck Surgery, Medical University of South Carolina, Charleston, South Carolina 29425 USA

[6]Division of Plastic Surgery, School of Medicine, University of South Carolina, Columbia, South Carolina 29203, USA

[7]Division of Plastic Surgery, Prisma Health Medical Group, Columbia, South Carolina 29203, USA

[8]Department of Biochemistry, University of South Carolina, Columbia, South Carolina 29208, USA

[9]Department of Biomedical Engineering, College of Engineering and Computing, University of South Carolina, Columbia, South Carolina 29208, USA

[10]Department of Obstetrics and Gynecology, University of California, Irvine, Irvine, California 92617, USA

[11]Departments of Surgery and Biomedical Engineering, Beckman Laser Institute and Medical Clinic, University of California, Irvine, Irvine, California 92617, USA

[12]Division of Biomedical Informatics, Cincinnati Children Hospital Medical Center, Cincinnati, Ohio 45229, USA

*Equally contributes to this work

Corresponding to:

Yunguan Wang, Department of Pediatrics, University of Cincinnati College of Medicine, Cincinnati, Ohio 45229, USA; email: yunguan.wang@cchmc.org

Wenbin Tan, Department of Cell Biology and Anatomy, School of Medicine, and Department of Biomedical Engineering, College of Engineering and Computing, University of South Carolina, Columbia, South Carolina, 29209, USA; email: wenbin.tan@uscmed.sc.edu

Running Title: NR2F2 Drives EndMT Acquisition in CM

Funding This work was supported by grants from the National Institute of Arthritis and Musculoskeletal and Skin Diseases of the National Institutes of Health (R00GM118885 and R01HL149762 to CFW, R01AR073172 and 1R21AR083066 to WT), Department of Defense (HT9425-23-10008 to WT), and the University of South Carolina School of Medicine Bridge Funding (to WT).

Declaration of interests: None

Summary

Background: Capillary malformation (CM) is a congenital vascular anomaly affecting the skin, mucosa, and brain, yet the understanding of its vascular pathogenesis remains limited.

Methods: We applied spatial whole-transcriptome profiling (GeoMx) and gene set enrichment analysis within CM lesions at single vasculature level. Differentially expressed genes were validated by immunofluorescence staining. Phosphoproteomics was profiled to uncover lesion-wide phosphorylation sites on proteins. Single-cell RNA sequencing was performed on CM-derived induced pluripotent stem cells (iPSCs) to determine differentiation trajectories of lesional vascular lineages. In silico gene perturbation was used to predict candidate genes for modulating vascular pathological progression, followed by functional validation in CM iPSC-derived endothelial cells (ECs) using a Tet-on system.

Results: A spatial transcriptomic atlas was constructed, and pathological landscape of individual CM vasculature was delineated. CM vessels exhibited hallmarks of endothelial-to-mesenchymal transition (EndMT), including disruption of adherens junctions (AJs), vascular identity transitions, and metabolic remodeling. Phosphoproteomics confirmed that differentially phosphorylated proteins were enriched in EndMT- and AJ-related pathways. Aberrant expression of venous transcriptional factor NR2F2 was observed in lesional ECs and correlated with progressive enlargement from capillaries to larger-caliber vessels containing multiple layers of smooth muscle cells (SMCs). In CM iPSCs, differentiation course yielded reduced ECs but increased SMCs. *In silico* knockout simulation predicted NR2F2 as a crucial regulator of facilitating SMC phenotype in CM. Consistently, enforced NR2F2 expression during iPSC differentiation suppressed endothelial markers while inducing SMC-associated genes.

Conclusions: Single CM vasculature displays pathological hallmarks characterized by EndMT and AJ disruption, leading to progressive vascular remodeling. NR2F2 functions as a central regulatory factor orchestrating the acquisition of the SMC phenotype, thereby representing a potential therapeutic target in CM.

Keywords: Capillary malformation, whole transcriptome atlas, induced pluripotent stem cells, endothelial cells, endothelial-to-mesenchymal transition, adherens junctions, NR2F2

Introduction

Congenital vascular malformations (VMs) are developmental disorders of the vasculature, affecting approximately 1.5% of the general population.[1] According to ISSVA classification, congenital capillary malformations (CMs) include several subtypes: cutaneous and/or mucosal CM (also known as port-wine birthmarks, PWB), CM with neurological involvement (Sturge-Weber syndrome, SWS), diffuse CM with overgrowth, reticulate CM, and certain forms of telangiectasia.[2] Among these, cutaneous CM is the most common, with a prevalence of 0.3%–0.9% in newborns.[3] Notably, about 25% of infants with forehead CM lesions are at elevated risk of SWS, characterized by ipsilateral leptomeningeal angiomatosis.[4] Clinical management of CMs remains challenging, often depending on lesion location and associated vascular anomalies. Pulsed dye laser (PDL) and photodynamic therapy (PDT) are standard treatments for cutaneous CM, showing comparable efficacy.[5,6] However, complete clearance is achieved in fewer than 10% of patients,[7] while approximately 20% of lesions are resistant to laser therapy.[8] Despite three decades of clinical use, laser-based approaches have yielded only limited improvements in outcomes.[9,10] A subset of CM endothelial cells (ECs) likely survive laser treatments, allowing the revascularization of lesional blood vessels after laser radiation.[11,12] This clinical inadequacy demands an understanding of the pathological phenotypes of CMs for the development of paradigm-shifting modalities.

Histologically, CM lesions display diverse vascular abnormalities, including proliferation of ECs and smooth muscle cells (SMCs), replication of vascular basement membranes, disruption of vascular barriers, and progressive dilatation of vasculature.[12,13] CM ECs exhibit stem-cell-like characteristics which have been posited as aberrant endothelial progenitor cells (EPCs),[12,14] leading to impairments of EC differentiation.[12] Several sporadic somatic mutations are shown to be related to vascular phenotypes of CMs, including the guanine nucleotide-binding protein, G alpha subunit q (GNAQ) (R183Q), G protein subunit alpha 11 (GNA11), phosphatidylinositol 3-kinase (PI3K), RAS P21 protein activator 1 (RASA1), STAM binding protein (STAMBP), and Ephrin type-B receptor 4.[2,15,16] Cutaneous CM and CM/SWS vasculature have GNAQ (R183Q) allelic frequencies ranging from 1 to 12 percent (about 4.7% on average) in skin lesions.[15] GNAQ (R183Q) is present in ECs or blood vessels,[11,17] connective tissues, hair follicles, and glands in CM lesions, suggesting that GNAQ (R183Q) pluripotent cells may give rise to multiple lineages in cutaneous CM.[11] EPCs with GNAQ (R183Q) can cause active phospholipase C (PLC) β3 signaling, increase angiopoietin-2 (ANGPT2), and produce enlarged capillary-like vessels.[18] Intriguingly, GNAQ (R183Q) is embryonically lethal, and mutant ECs likely persist through

mosaicism.[19] The low allelic frequency and mosaic distribution of GNAQ (R183Q) suggest that additional factors contribute to CM pathology. Furthermore, patient-derived induced pluripotent stem cells (iPSCs) generated in our laboratory, while lacking GNAQ (R183Q), nonetheless recapitulate clinically relevant vascular phenotypes *in vitro* and *in vivo,*[20,21] suggesting that epigenetic imprints within lesional cells may preserve disease phenotypes.

CM vasculature exhibits pronounced morphological and pathological heterogeneity, reflecting dynamic EC remodeling during disease progression. Increasing evidence points to a role for inflammation and metabolic reprogramming in CM pathology, as macrophages are frequently enriched in the perivascular environment of brain and skin lesions.[22,23] However, the underlying molecular signatures remain largely unknown. To address this, we performed spatial whole-transcriptome atlas profiling of single CM vasculature. Our analysis delineated the pathological landscape of individual vasculatures with signatures of endothelial-to-mesenchymal transition (EndMT) and revealed aberrant expression of nuclear receptor subfamily 2 group F member 2 (NR2F2/COUP-TFII), coinciding with progression of vasculature enlargement. These findings were corroborated by CM phosphoproteomics, which demonstrated enrichment of EndMT and adherens junction (AJ)–related pathways among differentially phosphorylated proteins. Functionally, CM lesion–derived iPSCs showed impaired endothelial differentiation but an expansion of SMC lineages. Importantly, induction of NR2F2 expression during the endothelial progenitor stage promoted EndMT-associated SMC phenotypes in ECs.

Methods

Tissue preparation

This study (#1853132) was approved by the Institutional Review Board at Prisma Health Midlands. Some biopsy samples were reported in our previous studies.[11,12,24] A total of 17 CM and 9 normal skin biopsy samples were used in this study, including (1) six surgically excised hypertrophic or nodular CM or biopsied CM/VM macular lesions and six de-identified surgically discarded normal skin tissues for GeoMx Spatial Whole Transcriptome Atlas (WTA) (Nanostring, Seattle, WA, USA), (2) six CM lesions and four normal skin controls for immunofluorescent (IF) staining assay to validate differentially expressed gene (DEG), and (3) five CM lesions and five normal skin controls for phosphoproteomics analysis. The biopsy tissues were 4% buffered formalin-fixed and parafilm-embedded (FFPE) for preparing sections (5 - 6 μm). The sample information was listed in supplementary table 1 Key Resource Table.

Single vasculature Spatial WTA by GeoMx Digital Spatial Profiler

De-identified FFPE sections were stained with DAPI. The region of interest (ROI) containing individual blood vessel was picked. The sections were permeabilized and hybridized using RNA specific probes labeled with a unique barcoding system. Flow cells were assembled, followed by automation of multiple rounds of reporter probe binding and fluorescence imaging for barcode readouts. Each RNA appeared as a single bright spot in the sample and were digitally quantified in the image.

Differential expression analysis was performed with pseudobulk analysis (one vs. the rest) using DecoupleR (v1.8.0) and pyDEseq2 (v0.4.12).[25] Absolute log fold change greater than 0.6 and FDR-adjusted P-value of 0.05 were used to select for differentially expressed genes (DEGs). Gene set enrichment analysis (GSEA) was performed with the package gseapy (v1.1.4 .) using the 'KEGG' and 'Hallmark' libraries from MsigDB.[26]

CM iPSC culture and iEC differentiation

The generation of CM and normal iPSC lines were reported previously.[20,21] Briefly, normal and CM iPSC lines were seeded into Geltrex-coated 6 well plate in mTeSR plus medium (STEMCELL, Cambridge, MA, USA) with 10μM Y27632. For iEC differentiation, the protocol was used in favor to arterial-like lineage commitment.[27-30] The details were described in supplementary method. For iPSC lines with integration of Tet-on system for inducible expression of NR2F2, the iPSCs were electroporated using pPB-cT3G-cERP2-NR2F2[31] (Addgene #192900, Watertown, MA, USA) plus

170 a Super piggyBac Transposase expression vector (SBI#, PB210PA-1, Palo Alto, CA, USA). The
171 cells were selected under 1.0-1.2 μg/ml puromycin to obtain the iPSC lines with a stable
172 integration of Tet-on system. The NR2F2 expression was induced using doxycycline (Dox, 1
173 μg/ml) during the designated phase.

174 **Single-cell RNA sequencing (scRNA-seq)**

175 The samples were collected for scRNA-seq at the following iPSC differentiation stages: iPSC (day
176 0), mesodermal cells (MC, day 4), progenitor cell mixture including EPCs and smooth muscle
177 progenitor cells (SMPC) (day 8), and iECs (day 14). Parse Evercode™ single-cell library kit was
178 used for library construction (Pars Bioscience, Seattle, WA, USA). Samples with biological
179 duplicates per group were processed. Paired-end sequencing was performed on a NovaSeq 6000
180 system (Illumina, San Diego, CA, USA) for 50 K reads per cell. GSEA based pathway analysis
181 was performed using the python package gesapy (v 1.1.4). The 'prerank' function was used to
182 identify enriched pathways from DEG ranked by log foldchange. Pseudotime analysis was
183 conducted using Diffusion Pseudotime (DPT, included in the scanpy package), which leverages
184 the diffusion map framework to order cells along a continuum based on their transcriptional
185 similarity.

186 **Bulk ATAC-seq and regulatory gene network (RGN) construction**

187 Bulk ATAC-seq was performed on iECs using a kit from Diagenode (Denville, NJ, USA) with
188 detailed description in supplementary method. Bowtie2[32] was used for ATAC-seq alignment and
189 MACS2[33] for peak calling. The ATAC-seq heatmap was generated using Galaxy platform.[34]

190 Gene Regulatory Network (GRN) and Transcription Factor (TF) analyses were performed
191 using CellOracle (v 1.18.0)[35], following procedures outlined in the CellOracle (https://morris-
192 lab.github.io/CellOracle.documentation/tutorials/index.html). Base GRNs were constructed using
193 bulk-ATAC sequencing data from the same cell samples, providing a foundation for inferring
194 regulatory interactions between TFs and their target genes. CellOracle integrated this information
195 with single-cell gene expression data to refine the GRN and identify key TFs driving cellular states
196 and transitions. To further investigate the functional roles of these TFs, knockout (KO) simulations
197 were conducted using CellOracle.

198 **Statistical analysis**

199 Student's t-test was performed to evaluate the statistical differences between CM and normal
200 control data sets. For nonparametric data, Mann-Whitney U Test was used. Data was presented
201 as "mean ± S.D." $p < 0.05$ was considered statistically significant.

202

203 **Results**

204 **WTA signatures for CM blood vessels**

205 A total of 123 regions of interest (ROIs), each containing a single blood vessel, were collected for
206 GeoMx WTA analysis. Validation using UEA1 or SMA immunohistochemistry identified seven
207 ROIs containing non-blood vessel structures, which were excluded. An additional 23 ROIs with
208 fewer than 180K aligned reads were removed for quality control, yielding 65 CM vessels (n = 6
209 patients) and 28 normal vessels (n = 6 subjects) for downstream analysis (Fig. 1A). Morphological
210 parameters assessed per ROI included nuclear counts, average blood vessel wall thickness
211 (BVWT, μm), blood vessel wall area (BVWA, μm^2), aligned reads per nucleus, and distance from
212 the epidermis (Supplemental Table 2). Based on these features, vasculature was categorized into
213 five groups (Fig. 1B, C): (1) normal capillaries/venules (17 ROIs), (2) normal small arterioles (11
214 ROIs), (3) small-thin CM vessels (BVWA < 10,000 μm^2; 28 ROIs), (4) large-thin CM vessels
215 (BVWT < 70 μm, 1–2 cell layers, BVWA > 10,000 μm^2; 11 ROIs), and (5) large-thick CM vessels
216 (BVWT > 70 μm, >3–4 cell layers, BVWA > 10,000 μm^2; 26 ROIs).

217 There were 467 upregulated and 136 downregulated DEGs in CM as compared to normal
218 vasculatures (Fig 1D, Supplemental Fig 1). Single vessel (e.g., each ROI) Gene Set Enrichment
219 Analysis (svGSEA) showed dysregulated pathways mainly involved vascular development
220 (angiogenesis, Notch signaling, Hematopoietic cell lineage, and hedgehog signaling) and EndMT
221 related biological processes (inflammatory responses, cell junctions and adhesion, and
222 hypoxia/ROS signaling) (Fig 1E, Supplemental Fig 1).

223 **Endothelial NR2F2 coincides with CM pathological progression**

224 CM ECs displayed features of EPCs,[12,14] co-expression of both venous and arterial biomarkers,
225 and loss of arteriole-like vasculature, indicating impaired arterial differentiation.[12] The WTA data
226 identified many DEGs related to venous (NR2F2, TMSB10, JUND), arterial (ASS1, S100A4,
227 TM4SF1, ELN), and progenitor (CD44, NOTCH3, KLF2, ENG) biomarkers (Fig 1F), suggesting
228 disrupted vascular lineage determination in CM.

229 The IF validation of cellular colocalizations and patterns of these DEGs related to EC and EPC
230 biomarkers were shown Supplemental Figs 2-3. Of note, NR2F2 is a TF for determining venous
231 identity,[36] and ASS1 is a post-capillary arterial biomarker in human dermal vasculature.[37] We next
232 performed an IF validation crossing CM vasculatures with different sizes in patient biopsies.
233 NR2F2 was found in nuclei of venous ECs while ASS1 was found only in arterial ECs in normal
234 dermal vessels (Fig 2A). Scattered SMCs showed a strong nuclei NR2F2 expression in
235 perivascular regions in both venules and arterioles (Fig 2, Supplemental Figs 4 and 5). In lesional
236 vasculatures with small sizes, many ECs co-expressed NR2F2 and ASS1 (Fig 2B, Supplemental
237 Fig 4). In intermediate-sized lesional vessels, there were several expression patterns in ECs
238 within single vessels: NR2F2 positive, ASS1 positive, and weak positive or negative for both
239 biomarkers (Fig 2B, Supplemental Fig 4), demonstrating a dynamic heterogeneity of (1) presence
240 of both venules and arteriole-like ECs within one vessel, and (2) co-existing of both venous and
241 arterial signatures in the same ECs. However, in thick, large-thick vessels with multiple layers of
242 SMCs, only NR2F2 was observed in the nuclei of many ECs but not ASS1 (Fig 2B, Supplemental
243 Fig 4). Neither NR2F2 nor ASS1 was observed in ECs in large-thin vessels with one or two layers
244 of SMCs. The proportion of ECs with positive NR2F2 nuclei per vessel in CM was significantly
245 higher than normal dermal blood vessels (Fig 2C). CM ECs express stem cell marker CD133.[12]
246 CD133 was localized in plasma membranes and NR2F2 was in nuclei in CM ECs (Supplemental
247 Fig 5), consistent with progenitor-like states. The dynamics and transition patterns of endothelial
248 NR2F2 were outlined in Fig 2D, coinciding with progressive enlargement of lesional vasculature.

249 svGSEA highlighted enrichment of lipid metabolism pathways (Fig. 1E). IF staining validated
250 altered expression of APOE and FADS2, two regulators of endothelial lipid metabolism. APOE
251 involves in endothelial dysfunction and FADS2 is expressed in dermal ECs engaging cholesterol
252 synthesis.[38,39] In normal skin, dermal capillaries or venules expressed low or moderate levels of
253 FDAS2 but not APOE; normal dermal arterioles expressed high levels of both APOE and FDAS2
254 ($APOE^H/FDAS^H$, Supplemental Fig 6). In CM lesions, three types of vessels were observed, low
255 levels of APOE and high levels of FDAS ($APOE^L/FDAS^H$), high levels of APOE and low levels of
256 FDAS $APOE^H/FDAS^L$, and $APOE^H/FDAS^H$ (Supplemental Fig 6), suggesting heterogeneous
257 metabolic reprogramming linked to impaired vascular lineage specification.

258 **Molecular signatures for enlarged CM blood vessels**

259 Principal Component Analysis (PCA) of GeoMX samples revealed distinct clustering between
260 normal and CM vessels (Fig 3A). During development, both dermal arterioles and venules are
261 differentiated from primitive capillary plexus (PCP).[40,41] In default, PCP is thought to develop into

262 a venule; while turning off venule specific genes and switching on arteriole specific genes will
263 drive dermal PCP differentiation into arterioles.[40] The normal arteriole samples were a part of
264 cluster within capillary/venule samples, reflecting normal PCP-to-arteriole differentiation. The
265 samples of CM big-thin (group 4) and big-thick (group 5) formed two separate clusters within the
266 small CM vessels (group 3) (Fig 3A).

267 We then performed subgroup comparisons between CMs (groups 3-5) and normal ones
268 (groups 1-2) (Supplemental Figs 7-13). There were 59 downregulated and 362 upregulated DEGs
269 in big-thick (group 5) versus big-thin CM vessels (group 4), including NR2F2 and many vascular
270 remodeling biomarkers (Fig 3B, Supplemental Fig 14). The svGSEA demonstrated that junction
271 pathways, EndMT, Notch, Hedgehog, and angiogenesis were significantly enriched in small CM
272 vessels (group 3) versus normal dermal capillaries/venules (group 1) (Fig 3C), suggesting their
273 functional involvements of differentiation. Inflammatory pathways (hypoxia, ROS, and TGFβ) and
274 tight junctions (TJs) were significantly enriched in big-thick versus big-thin CM vessels (Fig 3C),
275 implicating their functions in EC remodeling and disease progression. Interestingly, AJs were
276 significantly dysregulated across both comparisons (Fig 3C). Some presentative DEGs for big-
277 thick or big-thin CM vessels were shown in Fig 3D. IF validation showed that MYOZAP was
278 observed in both ECs and SMCs. It exhibited fragmented and distorted immunostaining patterns
279 in big-thick versus big-thin vessels (Supplemental Fig 15). IL23A1 expression was mainly
280 observed in SMCs but not ECs with similar immunostaining signal intensities in both types of CM
281 vessels (Supplemental Fig 15). We next used the blood vessel wall area (BVWA) as the
282 morphological index of blood vessel thickness and size. The correlation analysis showed that
283 BVWA was significantly correlated with scGSEA scores of hypoxia, ROS, and AJs (Fig 3F),
284 suggesting their roles in the pathological progression of CM blood vessels with thick versus thin
285 walls.

286 **Junctional impairment as an EndMT phenotype in CM**

287 SvGSEA showed EndMT was enriched in the CM vasculature compared with normal dermal blood
288 vessels (Fig 1E). One landmark phenotype of EndMT is dysregulations of EC-EC junctions
289 including TJs and AJs. We performed re-analysis of our existing TEM data of CM vessels.[13,42] CM
290 ECs showed a wide variety of impairments of TJs and AJs, including fragmented and tortuous
291 morphology, reduction or breakdown of electron density, widened AJ spacing, and absence of
292 entire junctional structures (Fig 4A, B). The overall ratios of impaired endothelial TJs and AJs in
293 CM lesions (83.99% ± 24.66%, n= biopsies from 12 patients) were significantly higher than the
294 baseline in normal skins (4.66% ± 8.77%, n= biopsies from 12 subjects, $p<0.0001$) (Fig 4C). Half

295 of the AJs (49.9%) in CM vasculatures versus 4.1% AJs in normal dermal vessels, showed
296 junctional spacing larger than 20 nm between adjacent ECs (Fig 4D, E; $p<0.0001$).

297 To further characterize the impairments of AJs in CM vasculatures, we examined the
298 transcriptime atlas of AJ-related factors including CDH5, CTNND1, CTNNB1. Both CTNND1 and
299 CTNNB1, but not CDH5, were significantly upregulated in CM blood vessels than normal vessels
300 (Fig 4F). The ratios of CDH5 to CTNND1 or CTNNB1 per vessel were significantly lower in CM
301 vessels than in normal vessels (Fig 4G). IF staining showed the co-locolization of both CTNND1
302 and CDH5 among EC-EC contacts (Supplemental Fig 16), further valiation was performed by
303 immunoblotting using cell lysate from the whole biopsy skins (Supplemental Fig 17). These data
304 demonstrate molecular bases underlying AJ impairments in CM vasculature.

305 We next validated the CTNND1 patterns in lesional blood vessels using IF staining. Normal
306 dermal capillary and venous ECs are flattened with orientations along the vessel's long axis with
307 intact cell-cell junctions (Figs 5A, B). CM ECs exhibit various morphological phenotypes: (1)
308 flattened shape ECs orient along the vessel's long axis, and (2) cuboidal shape ECs orient
309 perpendicularly along the vessel's long axis with frequently impaired EC-EC contacts (Figs 5C-
310 H). Both types of ECs can be found in CM vasculature of all sizes. Normal human dermal capillary
311 ECs had either barely detectable CTNND1 IF signals [Type 1 or normal 1 (N1)] (Fig 5A,
312 Supplemental Fig 18A) or puncta CTNND1 ($CTNND1^{pn}$) [Type 2 or normal 2 (N2)] among normal
313 venous EC AJs (Fig 5B; Supplemental Fig 18B). Occasionally, a few $CTNND1^{pn}$ ECs were found
314 in the lesions (Supplemental Fig 18C; 2). In general, CM ECs in flattened shapes had CTNND1
315 IF signals covering the basal membranes ($CTNND1^{bm}$) (Type 3; Fig 5C; 3; Supplemental Fig 18);
316 while CM ECs in cuboidal shapes usually showed CTNND1 IF signals on the lateral membranes
317 ($CTNND1^{lm}$) (Type 4; Fig 5C; 4; Supplemental Fig 18) or the lateral basal membrane ($CTNND1^{lb}$)
318 (Type 5; Fig 5G; 5; Supplemental Fig 18). Some ECs with a full transition of columnar shape
319 exhibited an extended lateral membrane CTNND1 pattern ($CTNND1^{elm}$) (Type 6; Fig 5E; 6;
320 Supplemental Fig 18). These EC morphological features suggest that $CTNND1^{elm}$ is a
321 pathologically advanced varaint of $CTNND1^{lm}$. A few ECs developed a pattern of CTNND1 in all
322 membranes ($CTNND1^{all}$) (Type 7; Fig 5G; 7; Supplemental Fig 18). We did not find any obvious
323 CTNND1 IF signals in SMCs. This data suggests that heterogenous CTNND1 patterns present a
324 snapshot of the dynamics of CM EC remodeling during disease progression.

325 **Vascular identity transition as an EndMT phenotype in CM**

326 The second landmark phenotype of EndMT is the cellular transdifferentiation in which ECs
327 partially lose their identity and acquire mesenchymal cell-like features, including a spindle-
328 shaped, elongated morphology (such as remodeled ECs with CTNND1 patterns of types 4 to 7)
329 or/and the acquisition of contractile properties. The representative EndMT related DEGs,
330 including ZEB2, TIMPs, IGFBPs, BMP1, MYLs, and TAGLN (a.k.a., SM22) were shown in Fig 1G.
331 We observed active intermediary EndMT zones within lesional vessels (Fig 6A, B). Such an
332 EndMT zone was formed by several ECs exhibiting cuboidal morphology with CTNND1^{lm} (type 4)
333 and CTNND1^{elm} (type 6) patterns. They presented some SMC phenotypes, e.g., expression of
334 aSMA (Fig 6C, supplemental Fig 19), suggesting the acquisition of myogenic tone. These
335 remodeled ECs present both EC and SMC biomarkers, demonstrating an active and intermediary
336 EndMT remodeling phase in lesional blood vessels.

337 Metabolic remodeling is another EndMT landmark phenotype. We next validated several DEGs
338 related to EndMT and metabolic remodeling using IF staining in CM vasculature, including VIM,
339 MYH9, TWIST1, TM4SF1, SERPINE1, TIMP3, Annexin V, eNOS, LRP1, SPARC, Ki67, GCLM,
340 S100A4, and HIF1α (Supplemental Figs. 5, 20, 21 and 22). In addition, the transcripts of
341 Collagens 1, 3, 4, 5, 6, and 14, another major category of EndMT biomarkers, were systemically
342 and significantly upregulated in CM vessels compared with normal dermal vessels (Supplemental
343 Fig 23A).

344 **Phosphorylated modulations of junctional proteins in CM**

345 Next, we screened the global activation of cellular signalings in CM lesions by mass spectrometry
346 (MS) to reveal phosphoproteomics and identify differentially expressed phosphorylated peptides
347 (DEP) (n=5 normal and 5 patients). A total of 2,044 phosphorylated proteins (including 4,779
348 phosphorylated sites) were identified with high confidence (localization probability > 0.75). The
349 relative quantitation of DEPs was divided into two categories: up-regulation (fold-change (FC) >
350 1.5 and $p < 0.05$) and down-regulation (FC < 0.667 (1/1.5) and $p < 0.05$). There were 203
351 upregulated DEPs (158 proteins) and 100 downregulated DEPs (88 proteins) in CM lesions
352 compared with the normal control skins (Fig 6D; Supplemental table 3). Approximately 51 out of
353 158 upregulated phosphorylated proteins had biological functions entangled to EMT/EndMT and
354 its related cell-cell junction, Rho GTPase cycle, and anchoring junction (Fig 6E). Other enriched
355 functional groups of DEPs included inflammation, cell migration, and cytoskeleton (Fig 6E), which
356 were also interactive with EndMT. The representative phosphorylated cell junction proteins in the
357 lesions were CTNND1, TJP1, GJA1, and JCAD (Fig 6F). In particular, CTNND1 had DEPs at
358 S230, S352, and S346, exhibiting 2.3, 3.7, and 8.9-fold increases compared to the control skin

359 (p=0.03, 0.01, and 0.002), respectively (Fig 6F). The profound DEP signatures also enriched in
360 GTPases, for example, ARHGAP32 (S706), ARHGAP1(S51), RALGAPA1(S860), ARHGEF17
361 (S735), and RALGPS2 (T361) in CM lesions than in normal skin (Fig 6G). Functional analysis of
362 DEPs showed the convergence of pathways in cell-cell junctions, anchoring junctions, Rho
363 GTPases, EMT/EndMT, hypoxia signaling, and inflammatory responses (Fig 6E, Supplemental
364 Fig 23B), consistantly with GeoMx WTA data.

365 **Impaired trajectory of CM iPSC differentiation into iECs**

366 We next performed scRNA-seq analysis to gain mechanistic insight into the CM pathological
367 progression. Samples were collected on days 0, 4, 8, and 15 during differentiation course from
368 iPSCs to iECs (Fig 7A). Ten major distinct populations, e.g., iPSC, iPSC_MC, MC_1, MC_2,
369 MC_3, SMPC, MC_EPC, SMC_1 (contractile phenotype), SMC_2 (synthetic phenotype), and EC
370 were clustered (Figs 7B-C, Supplemental Fig 24A). The associated biomarkers of each cluster
371 were plotted in Fig 7D. We next compared the differentiation trajectories of normal and CM
372 samples using pseudotime analysis. Both normal and CM iPSCs showed two distinct
373 differentiation pathways, e.g., endothelial lineage and SMC lineage (Fig 7E). The differentiation
374 of endothelial lineage was observed in a pathway from clusters of iPSC_MC, MC_1, EPC, to EC
375 (Figs 7F, G). While the differentiation of SMC lineage followed the track from clusters of iPSC_MC,
376 MC_SMPC, SMC_2, to SMC_1 (Figs 7 H, I). CM iPSC yielded a lower percentage of iECs (25.9%
377 versus 39.6%) but resulted in a higher ratio of iSMC lineages (SMC_1 plus SMC_2: 14.1% versus
378 8.6%) than normal ones (Figs 7F-I). Our iEC differentiation protocol is in favor of arterial lineage
379 commitment, demonstrating by high level expression of arterial biomarkers in iECs including
380 CXCR4, Hey1, Hey2, NOTCH1, DLL4, and EFNB2 (Fig 7D, Supplemental Fig 24B). These data
381 suggest that CM iPSCs have a reduction in arterial EC lineage differentiation but an enhancement
382 in SMC lineage determination (Fig 7J), which is consistent with our previous report showing
383 impairments of arterial differentiation in CM vasculature.[12]

384 To identify potential TFs underlying these differential impairments of CM iPSCs, we
385 constructed base GRNs of normal and CM iECs from the bulk ATAC-seq data (Fig 8A). The
386 degree centrality calculated using CellOracle (v 1.18.0) was used to rank the top TFs through
387 GRNs in normal and CM clusters of MC_1, EPC, EC, SMPC, SMC_2, to SMC_1 (Figs 8B, C;
388 Supplemental Figs 24C). To explore the role of TF activity on cell-specific gene expression
389 profiles, we performed *in silico* KO analysis using CellOracle. In each perturbative simulation, the
390 changes of vector field, a metric indicating the shift of cell identity, and perturbation score (PS), a
391 metric indicating the strength of shift, were used to predict the KO effect of individual TFs. A

392 systemic KO simulation identified top TFs with greater or less impacts on cell identity shifts in
393 each cluster in CM and control (Figs 8B, C; Supplemental Figs 24C). There were a handful of TFs
394 that overlapped with the DEGs from GeoMx data, including KLF2, NR2F2, EPAS1, NR4A1, ID1,
395 ID4, FOS, HEY2, TAL1, JUN, MSX2, PAX8, NPAS3, MEIS3, and RFX2 (Figs 8D-I; Supplemental
396 Figs 25 and 26). For example, KLF2 KO suppressed MC_EPC cluster formation but promoted
397 differentiation from MC_EPC to EC cluster in CM compared with the control (Figs 8D, H). NR2F2
398 and EPAS1 KOs exhibited inhibition on SMPC cluster in both CM and control (Figs 8E, F, H).
399 NR4A1 KO inhibited SMPC cluster in the control but promoted SMPC cluster in the CM (Figs 8G,
400 H). KLF2, NR2F2, and EPAS1 were upregulated, whereas NR4A1 was downregulated in GeoMx
401 profile (Fig 1F, Fig 8I). Together, these data suggest that upregulation of NR2F2 and EPAS1, and
402 downregulation of NR4A1 may drive the SMC phenotype development in CMs. The KO
403 simulations of other overlapping TFs in GeoMx DEGs were performed. In summary, the following
404 TFs were predicted to have more engagements in EC lineage development in CM than control:
405 ID4, FOS, HEY2, JUN, TAL1, and NPAS3. While the TFs including MSX2, RFX2, MEIS3, NPAS3,
406 and PAX8 contributed more to SMC phenotype development in CM than in the control
407 (Supplemental Figs 25 and 26).

408 **NR2F2 promotes iECs acquiring EndMT-like SMC phenotypes**

409 NR2F2 is a master TF that determines venous identity and is a major driver for EMT in epdithelial
410 cells. The above NR2F2 KO simulation suggested that NR2F2 promotes SMC phenotype in CM.
411 This led us to explore the role of NR2F2 in the acquisition of EndMT in iECs. We integrated a Tet-
412 on system to induce NR2F2 expression in normal and CM iPSC lines. Dox was added from day
413 5 (EPCs) to 14 to induce NR2F2 overexpression (Figs 8J, K). CM iECs showed higher basal
414 levels of some EndMT biomarkers such as TAGLN (a.k.a., SM22), Calponin 1, and MMP2 (Figs
415 8K, L). Forced expression of NR2F2 resulted in decreases in many EC biomarkers, such as CD31,
416 CDH5, ANTXR1, and DLL4 in CM iECs (Figs 8K, L). It also led to increases in SMC biomarkers
417 such as TAGLN and calponin 1 in both CM and CTL iECs. Forced expression of NR2F2 also
418 upregulated MMP2 expressions in CTL iECs, reaching to its' basal level in CM iECs (Figs 8K, L).

419

420 **Discussion**

421 In this study, we have demonstrated that CM vasculature consists of differentially defective ECs.
422 Lesional ECs exhibit several landmark phenotypes of EndMT including AJs impairments, vascular
423 identity transitions and metabolic remodeling. CM iPSCs recapitulate an attenuation of EC lineage

424 differentiation but an enhancement in SMC phenotype development. Consecutive expression of
425 NR2F2 in CM progenitor cells can promote differentially defective ECs to acquire EndMT.

426 The first evidence showing inflammatory contributors to CMs was reported by Nasim et al.[22]
427 This study finds that enlarged blood vessels lack mural cells and their perivascular beds contain
428 phagocytic macrophages and neutrophils in brain CMs.[22] The immune cells such as macrophages
429 have been shown as major contributors to EndMT.[43,44] In our study, two types of big caliber
430 cutaneous blood vessels are shown in skin lesions: (1) thin ones devoid of SMCs, which are
431 similar to those enlarged ones in the SWS brain,[22] and (2) thick ones with replications of SMCs,
432 basement membranes, and extracellular matrix such as collagens, as a major vascular type found
433 in CMs. Some ECs in these vessels present predominant EndMT molecular phenotypes upon
434 acquisition of SMC features. Consistently, our WTA data shows a spectrum of inflammatory
435 pathways such as TGF-β, TNFα, ILs, and leukocyte transendothelial migration are upregulated in
436 cutaneous CMs. Soft tissue outgrowth is a clinical manifestation of cutaneous CM lesions
437 associated with EndMT. Our data indicate that lesional ECs likely contribute to fibrosis through
438 the following mechanisms. First, ECs can be direct sources of myofibroblasts through EndMT
439 phenotypical transition. Chronically activated fibroblasts (i.e., myofibroblasts) have been
440 recognized as the main cell population responsible for fibrosis in a variety of disorders.[45] For
441 example, dermal microvascular ECs from lesional skins in patients with systemic sclerosis present
442 an intermediate stage of EndMT, express both endothelial and myofibroblast markers, and display
443 a spindle-shaped appearance and a contractile phenotype *in vitro*.[45,46] Second, ECs can secrete
444 various proinflammatory factors to interact with immune cells and release profibrotic mediators to
445 activate fibroblasts. For example, Nasim et al. showed that ECs with the GNAQ (R183Q) mutation
446 can increase the expression of ICAM1, thereby enhancing the adhesion of immune cells on the
447 surface.[22] An increase in macrophage subset (MRC1/LYVE1) in both brain and skin CMs[22,23] has
448 suggested the contributive roles of inflammatory components. This study has found that
449 proinflammatory and profibrotic factors such as IGFBP4, 5, and 7 are upregulated in CM vessels,
450 further supporting this mechanism. More interestingly, Nasim et al. has found that there are
451 “sprouting vessels” in CM skin lesions.[23] We found similar “sprouting vessels” in this study.
452 Morphologically, the tip cells in the “sprouting vessels” exhibited advanced CTNND1 patterns.
453 Therefore, the tip cells in the CM “sprouting vessels” are likely invasive to the SMC layers under
454 an active EndMT process. Collectively, our data suggests that EndMT is detrimental to the
455 pathological progression of CMs.

NR2F2 is a master TF for venous identity.[36] In addition, the upregulation of NR2F2 increases ROS production[47] and results in fibrosis[48] and cardiomyopathy.[47] NR2F2 has been shown to facilitate the EMT by promoting cell invasion, migration, and expression of CDH2 and vimentin.[49] However, the role of NR2F2 in EndMT remains unclear. In this study, we demonstrate that NR2F2 is a driver for CM progenitor cells to acquire EndMT: (1) NR2F2 is constantly expressed in a subset of SMCs throughout CM vessels of all sizes; (2) NR2F2 KO simulation shows that NR2F2 can promote SMC phenotype development; (3) Nuclear NR2F2 is consecutively present in CM ECs throughout the disease small caliber vessels to thick large vessel development; and (4) Consecutive expression of NR2F2 can lead to EndMT acquisition in CM iECs. Our data suggest that hypoxia and ROS signaling are the driving pathways for EndMT in CMs. The overexpression of NR2F2 can increase ROS production.[47] Therefore, one possible potential cofactors of NR2F2 is the hypoxia/ROS pathway. This new research direction will be our future focus, and it will identify the cofactors in CM.

This study has several limitations. First, WTA data were obtained from single blood vessels containing a mixture of ECs and SMCs. Data generated was not from a single cell resolution, which impedes further analysis of cell-cell interactions. Second, GeoMx is a hybridization-based assay. It is less sensitive but less biased than PCR-based RNA-seq platforms. Therefore, it may fail to identify some genes that are dysregulated in CM lesions. Third, the NR2F2-mediated pathways that lead to the EndMT acquisition of CM ECs have not yet been identified. Fourth, the structural, dynamic, and functional aberrances of AJs, their interactions with NR2F2, and their roles in EndMT in CM lesions have not been explored. These will be the scope of our future investigations.

Figures:

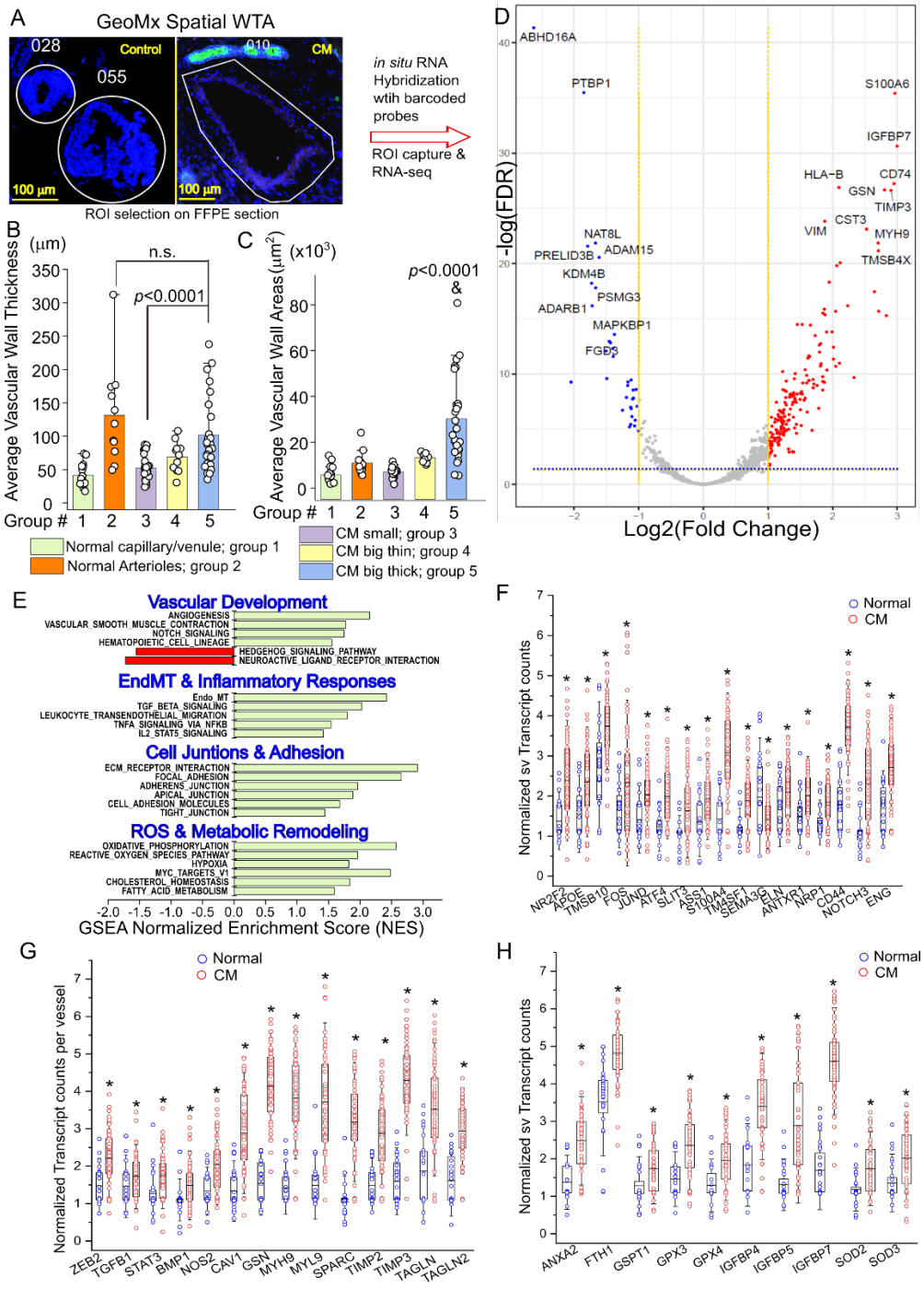

Figure 1 WTA profiles for CM vs normal vasculature: A, Each ROI image contains a single blood vessel from FFPE sections in normal control skin or CM lesion for WTA profiling using a GeoMx platform; B-C, Morphological features of blood vessels in ROIs; The profiled vasculatures were categorized into five groups based on their average vascular wall thickness and wall areas; D, Volcano plot for DEGs from WTA profiles of CM vs normal control blood vessels; Red or blue

dots in volcano plots: significantly up- or down-regulated DEGs, respectively (FDR < 0.05). E, Single vessel normalized enrichment score for GSEA (svNES_GSEA) showing the major dysregulated pathways in CM vs normal dermal vasculature; F-H, Representative DEG plots related to EC and EPC biomarkers (F), EndMT panel (G), and Hypoxia/ROS signaling (H). Each dot represents a single vessel. * FDR < 0.05.

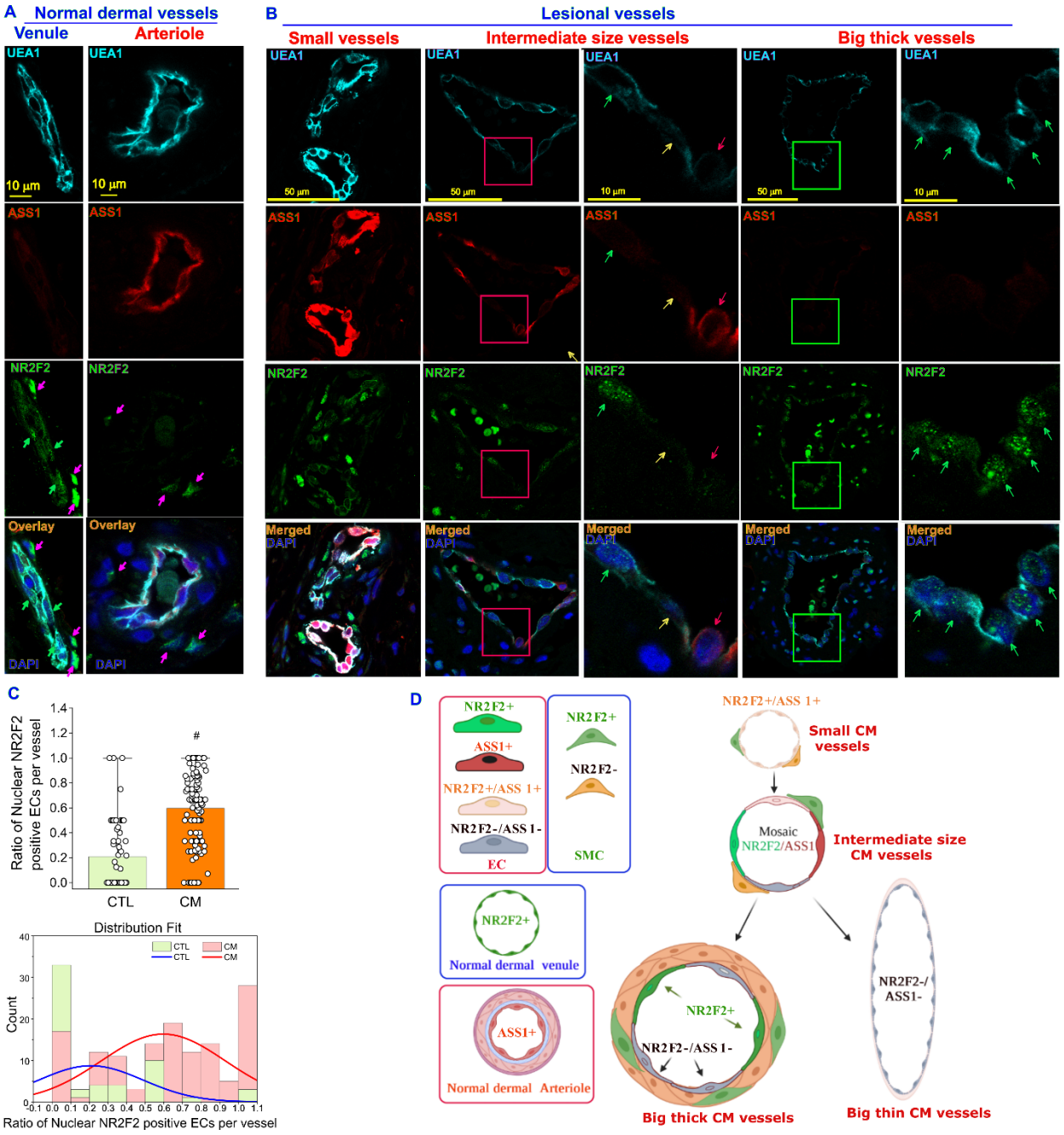

502 **Figure 2 Endothelial NR2F2 coincides with pathological progressions of CM vasculature**.
503 A, venous driver NR2F2 (green) was found in nucleus of ECs in normal dermal venous, but dermal
504 arterial biomarker ASS1 (red) was mainly present in arterial ECs in normal dermis. Some
505 scattered SMCs showed strong nucleus NR2F2 IF signaling in both venous and arterioles (pink
506 arrows). B, In small size CM vessels, the co-expression of ASS1 and NR2F2 were observed in
507 many ECs. In intermediate size vessels, ECs in one vessel could show heterogenous patterns of
508 NR2F2 (green arrows) positive, ASS1 (red arrows) positive, or negative for both biomarkers
509 (yellow arrows). In big dilated and thick lesional vessels, NR2F2 but not ASS1 was found in the
510 nucleus of many ECs. The 2nd panel of intermediate size or big size vessels is a high magnification
511 of the box area of each image in the 1st panel, respectively. UEA1 (cyan) staining was used to
512 show ECs. C, Quantitative analysis and distribution fit of the ratio of nuclear NR2F2 positive ECs
513 per vessel in normal skin as compared to CM. #, $p < 0.0001$. D, the dynamics and transition
514 patterns of nuclear NR2F2 in ECs coincides with progressive enlargement of lesional vasculature.

515

516

517

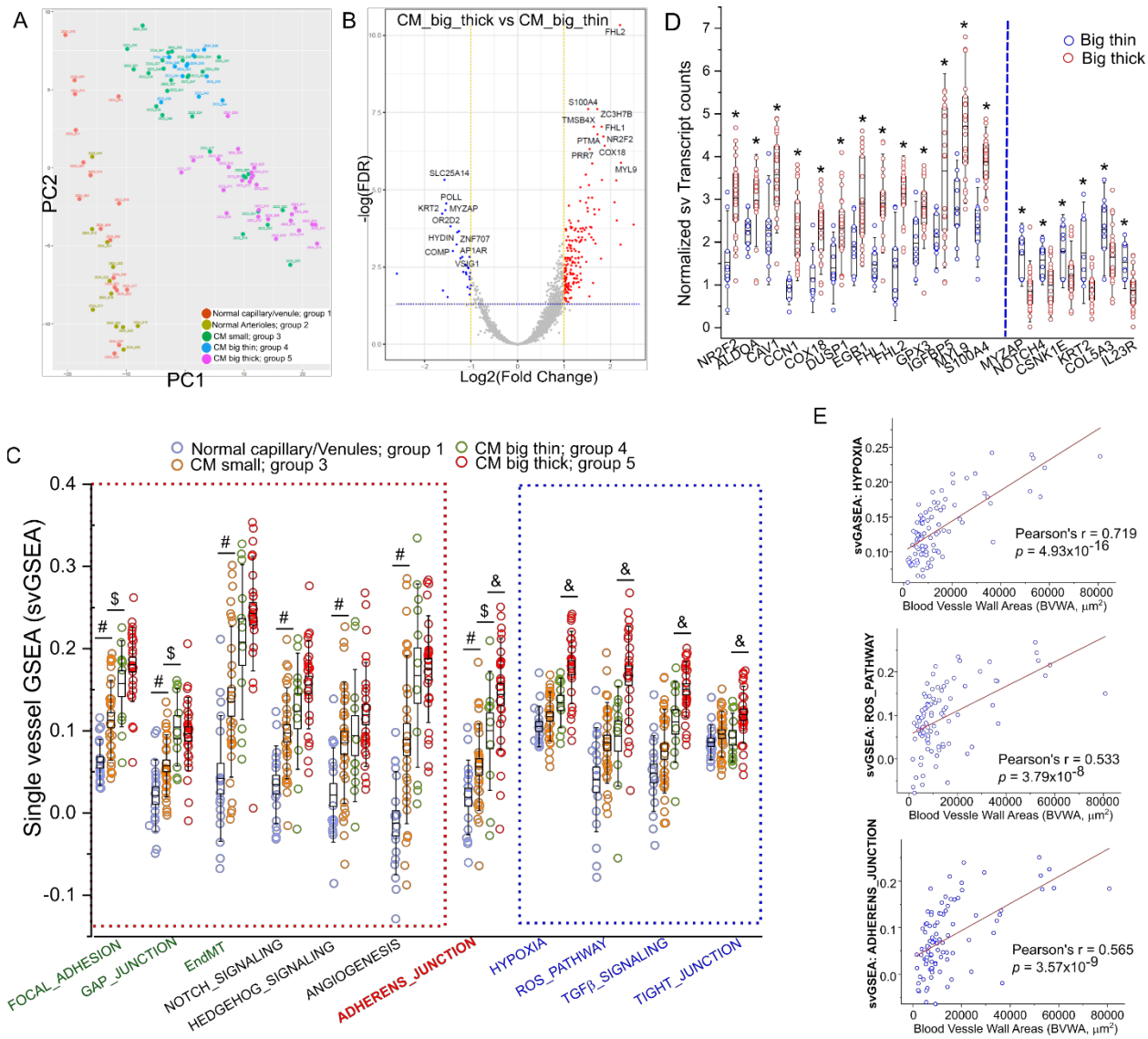

Figure 3: WTA profile comparison of big thick versus big thin CM vessels. A, PCA plot showing sample distances among all profiled blood vessels in ROIs from groups 1-5. B, Volcano plot for DEGs from WTA profiles of big thick versus big thin CM vessels; Red or blue dots in volcano plots: significantly up- or down-regulated DEGs, respectively (FDR < 0.05); C, Scattered plot showing svNES_GSEA for main pathways among groups; # group 3 vs group 1 with FDR < 0.05; $ group 4 vs group 3 with FDR < 0.05; & group 5 vs group 4 with FDR < 0.05; D, Representative DEGs of WTA profile comparison of big thick versus big thin CM vessels. * FDR < 0.05. E, Pearson correlation between BVWA and svNES_GSEA of hypoxia, ROS, and AJ pathways, respectively. Each dot in panels C-E represents DEG or GSEA from a single vessel.

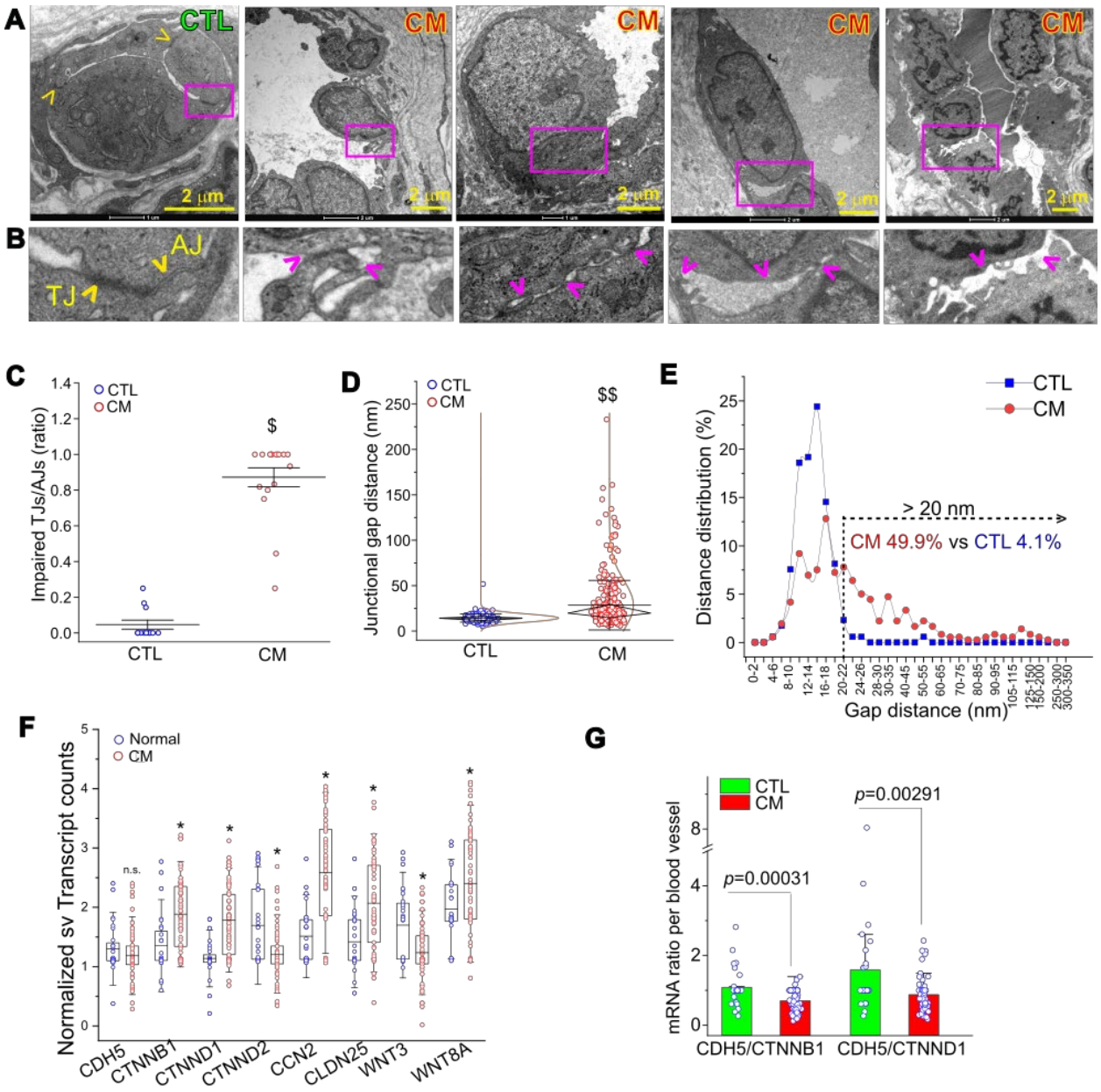

Figure 4: Impairments of AJs in CM vasculature. A, TEM showing the AJs among ECs from a normal dermal capillary and various types of fragmented and tortuous AJs among CM ECs with enlarged junctional spaces. B, The magnified box area from upper panel in (A) respectively. Yellow arrowhead: normal TJ and AJ; Pink arrowhead: impaired AJs. C, The ratio of impaired TJs and AJs over normal ones among control or CM vessels. Each dot represents one subject or patient. $ p<0.0001. D, Junctional gap distances in AJs from normal and CM vessels. $$ p<0.0001. E, The distribution of gap distances in AJs from normal vessels as compared to CM vessels. F, Scattered plot showing the normalized transcript counts of AJ-related genes in CM as compared to normal vessels. Data was from GeoMx WTA profile. n.s., no significance for CDH5; * FDR <

539 0.05. G, mRNA ratio of CDH5/CTNNB1 or CDH5/CTNND1 per blood vessel in control as
540 compared to CM lesions.

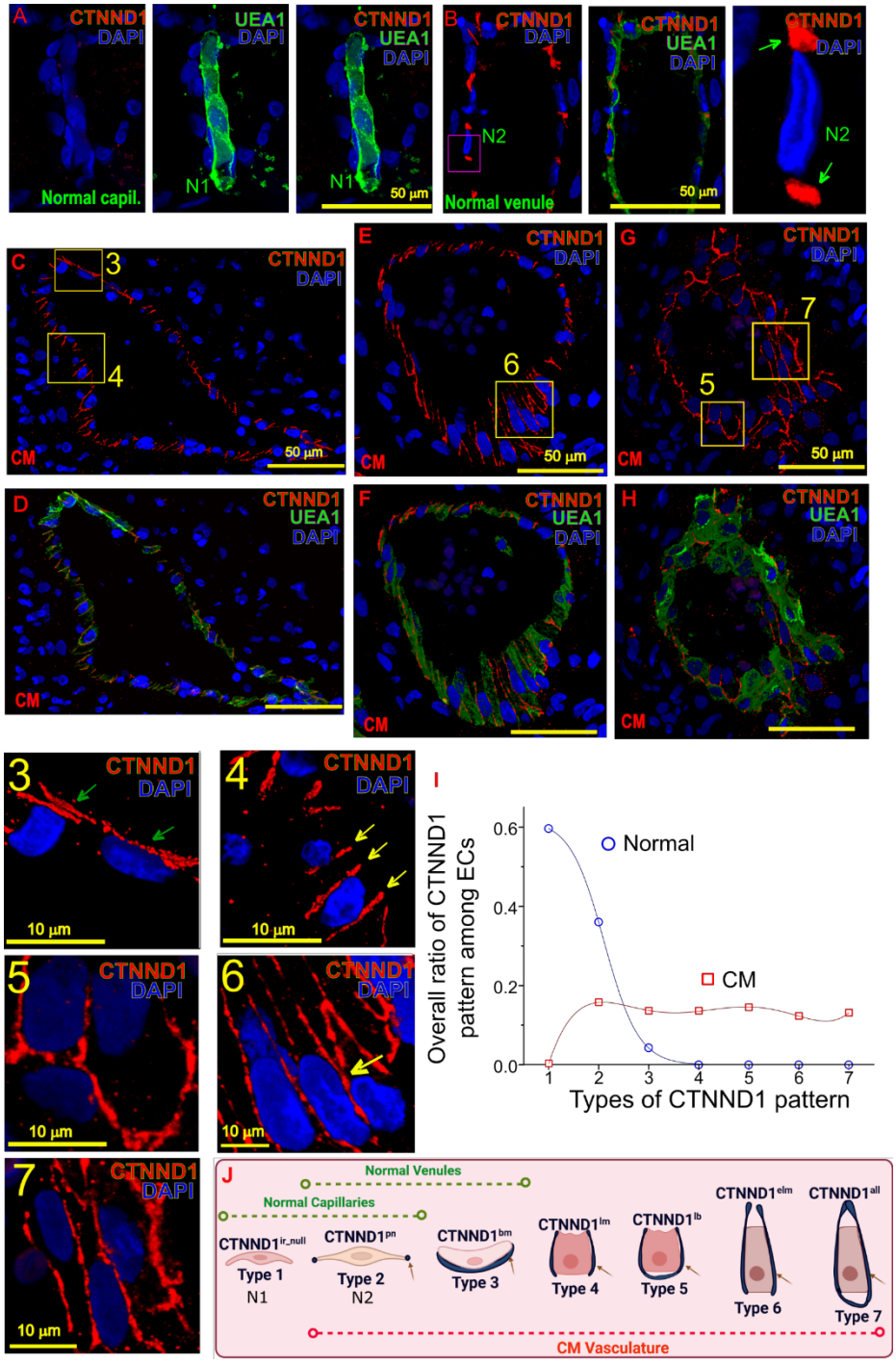

541

542 **Figure 5: CM ECs with heterogenous CTNND1 patterns reflecting dynamics of EC**
543 **phenotype remodeling**. A and B, Normal human dermal capillary ECs had either barely
544 detectable CTNND1 (red) IF signals (A, normal type 1, N1) or puncta CTNND1 (CTNND1^{pn}) (B,

normal type 2, N2) between normal venous ECs. The right panel showing a high magnification of the red box area of N2; C-H, CM ECs represent various patterns of CTNND1 among lesional blood vessels. Numbered boxed areas in (C), (E), and (G) are magnified and shown in the individual panels with the same number, presenting heterogenous types of CTNND1 patterns. UEA1 (green) staining was used to show the morphologies of vasculature in (D, F, and H). Z-stacks confocal images were processed for CTNND1 subcellular patterns. I, Overall ratios of various CTNND1 patterns among ECs in normal dermal and CM blood vessels. J, Predicted trajectory of endothelial CTNND1 patterns that reflects the diversity and dynamics of CM EC remodeling during disease progression.

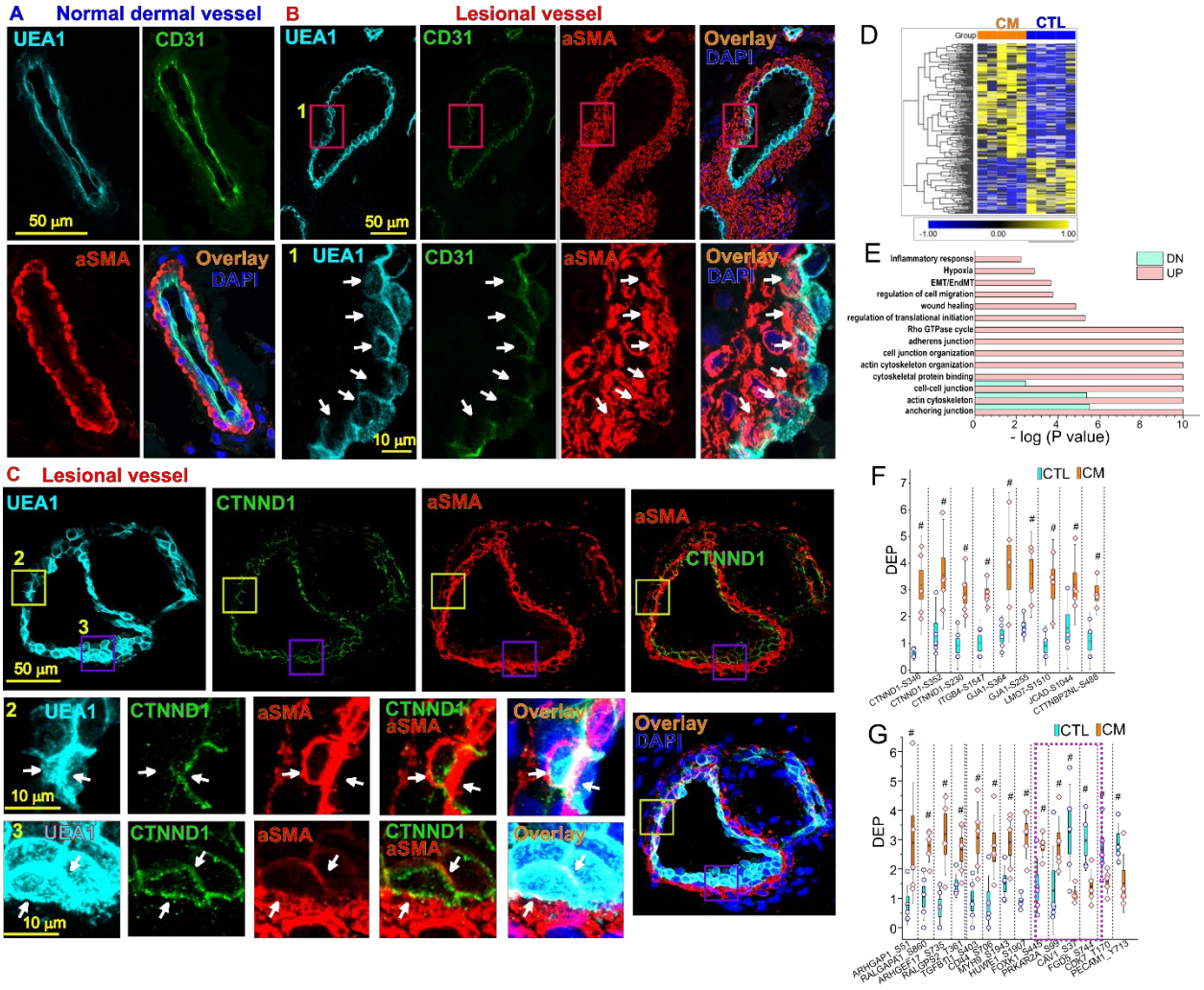

Figure 6: CM ECs undergoing EndMT hallmarks and phosphoproteomics profiles in CM lesions. A, A normal human dermal vessel exhibits distinct aSMA (red) signals in juxtaposition to

ECs showing by UEA1 (cyan) or CD31 (green); B, A CM lesional vessel develops an EndMT zone (red box 1) containing remodeled ECs (white arrows). Those ECs have acquired phenotypes of SMCs, e.g., expressing aSMA and showing cuboidal shapes. In (B), lower panels are a high magnification of the red box areas (box 1) in upper panels. DAPI: blue. C, ECs in active EndMT zones presenting various endothelial CTNND1 patterns in a CM vessel. Lower small panels 2 and 3 are a high magnification of the boxed areas with the same number in the upper panel showing endothelial CTNND1^{lb} (yellow box 2) and CTNND1^{all} (purple box 3, multiple layers of ECs) patterns. White arrowhead: the colocation of UEA1 (cyan), CTNND1 (green), and SMA (red). D, Heatmap data showing representative DEPs in CM lesions as compared to normal skin; E, Significantly enriched pathways involving DEPs' functions; F, Scattered plot showing DEPs of junctional related proteins including CTNND1 at S346, S352, and S230 sites in CM lesions vs normal controls (n=5 subjects); G, Scattered plot for some representative DEPs related Rho GTPases and endothelial functions.

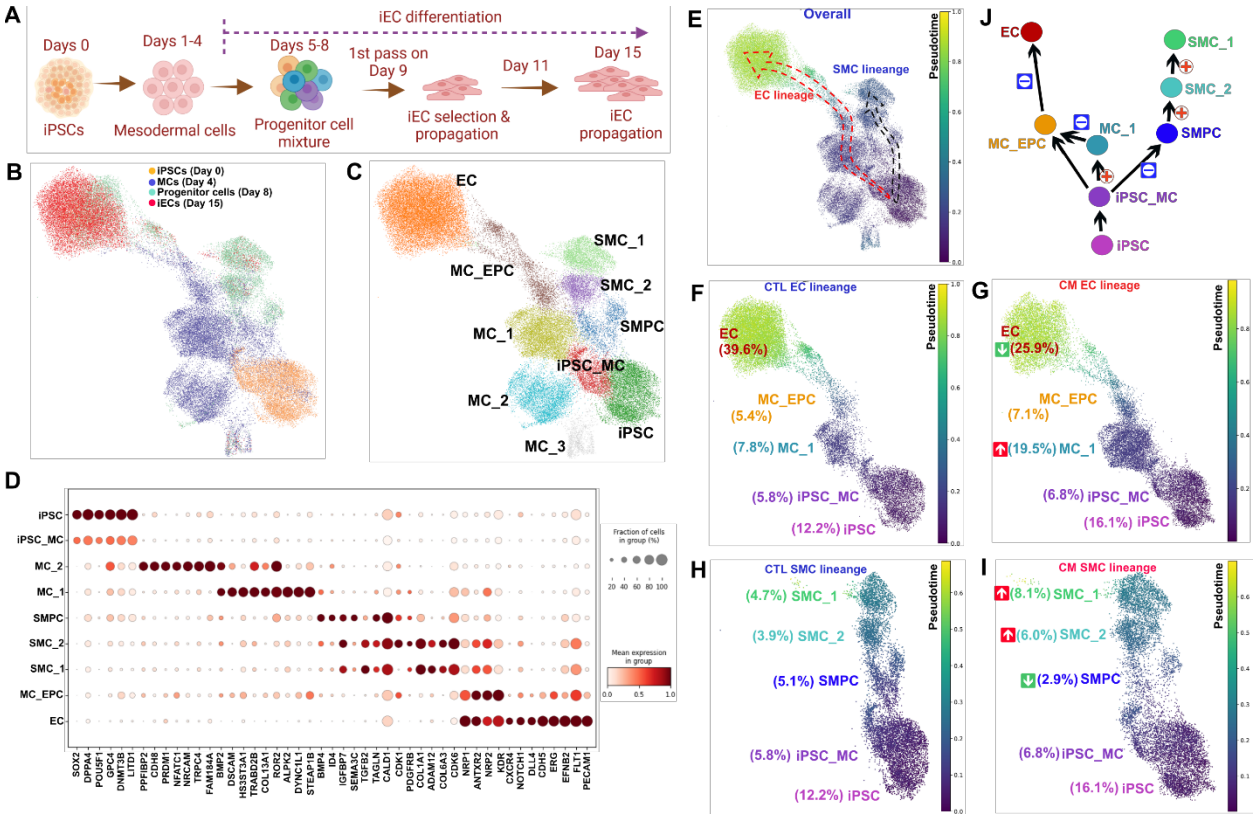

Figure 7: Differentiation impairments of CM iPSC to vascular lineages. A, Schematic of normal or CM iPSCs differentiation to iECs. Samples were collected on days 0, 4, 8, and 15 for

scRNA-seq analysis. B and C, UMAP showing the distributions of cell cultures among sampling times and cell types. D, Dot plot showing biomarkers for different clusters of cell types. E, Pseudotime analysis showing differential trajectories of EC and SMC lineages. F and G, Pseudotime analysis showing a differential stall of EC lineage in CM as compared to normal iPSCs with an increased MC_1 subpopulation but increased EC subset. H and I, Pseudotime analysis showing a differential enhancement of SMC lineage in CM as compared to normal iPSCs with increased SMC_2 and SMC_1 subsets. J, Schematic of differential trajectories and impaired paths in CMs.

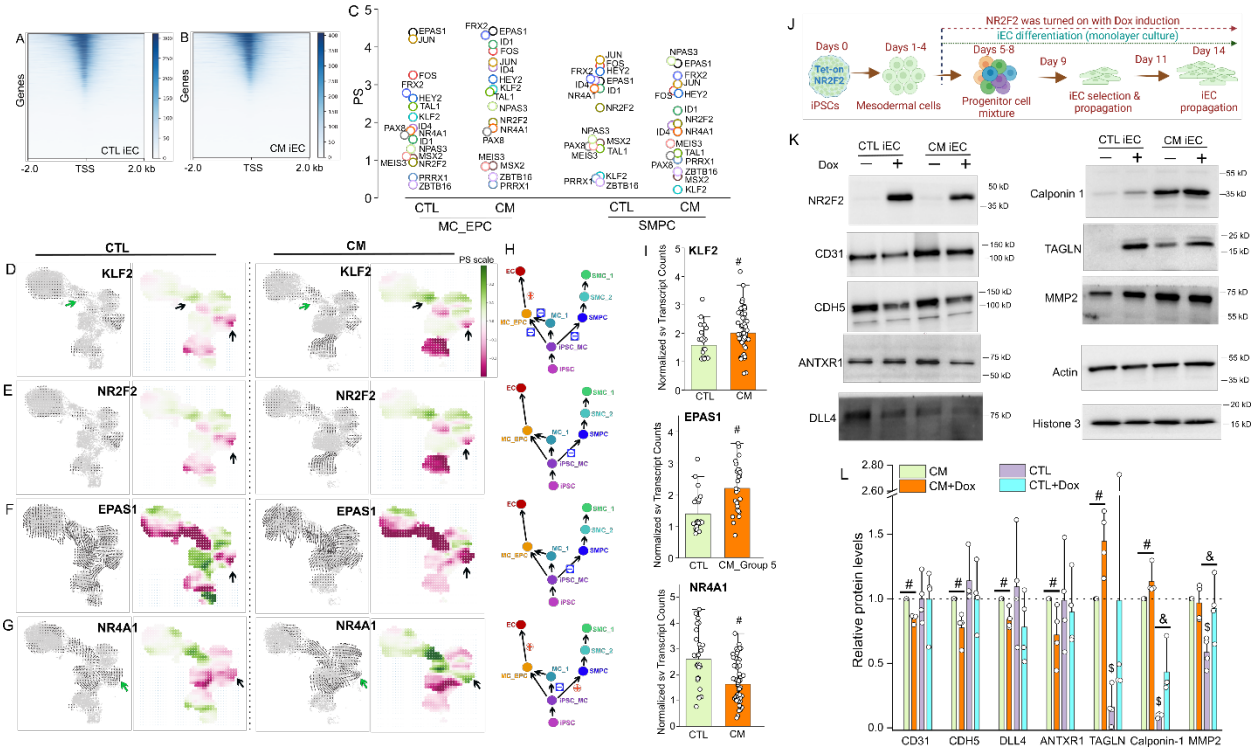

Fig 8: In silico gene perturbation and forced expression of NR2F2 promoting EndMT. A and B, Heatmaps showing enrichment at transcription start site (TSS) for the ATAC-seq profiles of normal (A) and CM iECs (B). GRN models were constructed from peaks files of ATAC-seq data. C, perturbation scores of representative TFs among GeoMx DEGs showing their impacts on cell identity shifts in clusters of MC_EPC and SMPC in CM and CTL through KO simulation. D-G, CellOracle simulation of cell-state transition in *Klf2* (D), *Nr2f2* (E), *Epas1* (F), and *Nr4a1* (G) KO simulation in CTL and CM. Summarized simulation vector field and the perturbation scores were shown, respectively. PS scale, green color indicates differentiation promoted; red color, differentiation suppressed with specific TF KO simulation. H, Schematic of impact on perturbative shifts for iEC or iSMC lineages with each specific TF KO simulation in CM and CTL. I, Single

vessel GeoMx profile of specific TFs in CM as compared to CTL. #, FDR < 0.05. J, Schematic of normal or CM iPSCs with integration of a Tet-on system to induce over-expression of NR2F2 with Doxycycline (Dox). Dox was added on day 5 to day 14 during iEC differentiation stages. K, Forced expression of NR2F2 at the stages from EPCs to iECs could cause reductions of EC biomarkers such as CD31, CDH5, DLL4, ANTXR1, and increases in EndMT biomarkers such as TAGLN, Calponin 1, and MMP2 in iECs. L, Relative protein levels of selective EndMT biomarkers. The basal level of each protein in CM iECs is set as 1 (dashed line). #, $p<0.05$ Dox versus mock in CM iECs; &, $p<0.05$ Dox versus mock in CTL iECs; $, $p<0.05$ basal level in CM versus CTL iECs. N=4 independent experiments. The average of normalizations to two housekeeping proteins β-actin and histone 3 is set as relative protein level.

Acknowledgement

We appreciate Dr. Raju Pillai and Dr. Lixin Yang in the Department of Pathology, City of Hope National Medical Center, Los Angeles for the assistance of GeoMx WTA experiments. We are very thankful for the support and assistance from the University of South Carolina School of Medicine Instrumentation Resource Core Facility (RRID:SCR_024955). The Galaxy server used for some calculations is partly funded by the German Federal Ministry of Education and Research BMBF grant 031 A538A de.NBI-RBC and the Ministry of Science, Research and the Arts Baden-Württemberg (MWK) within the framework of LIBIS/de.NBI Freiburg.

Database deposition

The scRNA-seq omics data has been deposited into the NCBI GEO (GSE295372). The GeoMx data has been deposited into the GEO (GSE297100). Data is available to the public.

Resource availability

Lead contact

Further information and requests for resources and reagents should be directed to and will be fulfilled by the lead contacts, Wenbin Tan (wenbin.tan@uscmed.sc.edu) and Yunguan Wang (yunguan.wang@cchmc.org).

Materials availability

Unique/stable reagents generated in this study are available from the lead contact Wenbin Tan (wenbin.tan@uscmed.sc.edu) with an MTA.

Data and code availability

The GeoMx WTA data, CM phosphoproteomic data, and iEC ATAC-seq data are deposited into the NCBI GEO or as supplemental materials that are available to the public.

The code is available from the lead contact Yunguan Wang (yunguan.wang@cchmc.org).

Author contributions

W.T. designed and supervised the study. Y.W. designed and supervised the bioinformatic analysis of the study. V.N., together with I.C., S.H., M.A., Y.R., L.P., performed GeoMx, IF, scRNA-seq, Western blot, phosphoproteomic, iPSC culture experiments. I.M. performed scRNA-seq, RGN, and KO simulation analyses. M.L.H., E.H.C., and H.I.F. performed patient consents and biopsy collections. A.G.J. performed phosphoproteomic analysis. Y.C.C., Q.L., D.F., C.F.W., D.C., J.S.N., A.G.J., and Y.W. contributed to data analysis, data interpretation, and manuscript revision. V.N. and W.T. drafted the manuscript with input from all authors.

Declaration of interests

The authors declare no competing interests.

Supplemental information

Supplemental method and discussion

Supplemental Figures 1-26

Supplemental tables 1-3

References

1. Eifert S, Villavicencio JL, Kao TC, Taute BM, Rich NM. Prevalence of deep venous anomalies in congenital vascular malformations of venous predominance. *J Vasc Surg*. 2000;31:462-471.
2. ISSVA. ISSVA Classification of Vascular Anomalies. *International Society for the Study of Vascular Anomalies* 2018;issva.org/classification.
3. Lever WF, Schaumburg-Lever G. *Histopathology of the Skin*. 7th ed. Philadelphia, PA: J.B. Lippincott Co.; 1990.
4. Waelchli R, Aylett SE, Robinson K, Chong WK, Martinez AE, Kinsler VA. New vascular classification of port-wine stains: improving prediction of Sturge-Weber risk. *Br J Dermatol*. 2014;171:861-867. doi: 10.1111/bjd.13203
5. Gao C, Nguyen V, Hochman ML, Gao L, Chen EH, Friedman HI, Nelson JS, Tan W. Current clinical evidence is insufficient to support HMME-PDT as the first choice of treatment for young children with port wine birthmarks. *Lasers Surg Med*. 2024;56:321-333. doi: 10.1002/lsm.23779
6. Aguilar G, Diaz SH, Lavernia EJ, Nelson JS. Cryogen spray cooling efficiency: improvement of port wine stain laser therapy through multiple-intermittent cryogen spurts and laser pulses. *Lasers Surg Med*. 2002;31:27-35. doi: 10.1002/lsm.10076
7. Nelson JS, Jia W, Phung TL, Mihm MC, Jr. Observations on enhanced port wine stain blanching induced by combined pulsed dye laser and rapamycin administration. *Lasers in surgery and medicine*. 2011;43:939-942. doi: 10.1002/lsm.21141
8. Savas JA, Ledon JA, Franca K, Chacon A, Nouri K. Pulsed dye laser-resistant port-wine stains: mechanisms of resistance and implications for treatment. *Br J Dermatol*. 2013;168:941-953. doi: 10.1111/bjd.12204
9. van Raath MI, Chohan S, Wolkerstorfer A, van der Horst C, Storm G, Heger M. Port wine stain treatment outcomes have not improved over the past three decades. *J Eur Acad Dermatol Venereol*. 2019;33:1369-1377. doi: 10.1111/jdv.15599
10. van Raath MI, Chohan S, Wolkerstorfer A, van der Horst C, Limpens J, Huang X, Ding B, Storm G, van der Hulst R, Heger M. Clinical outcome measures and scoring systems used in prospective studies of port wine stains: A systematic review. *PLoS One*. 2020;15:e0235657. doi: 10.1371/journal.pone.0235657
11. Tan W, Nadora DM, Gao L, Wang G, Mihm MC, Jr., Nelson JS. The somatic GNAQ mutation (R183Q) is primarily located in Port Wine Stain blood vessels. *J Am Acad Dermatol*. 2016;74:380-383. doi: 10.1016/j.jaad.2015.09.063
12. Tan W, Wang J, Zhou F, Gao L, Rong Y, Liu H, Sukanthanag A, Wang G, Mihm MC, Jr., Chen DB, et al. Coexistence of EphB1 and EphrinB2 in Port Wine Stain Endothelial Progenitor Cells Contributes to Clinicopathological Vasculature Dilatation. *Br J Dermatol*. 2017;177:1601-1611. doi: 10.1111/bjd.15716
13. Tan W, Zakka LR, Gao L, Wang J, Zhou F, Selig MK, Sukanthanag A, Wang G, Mihm MCJ, Nelson JS. Pathological Alterations Involve the Entire Skin Physiological Milieu in Infantile and Early Childhood Port Wine Stain. *Br J Dermatol*. 2016;177:293-296. doi: DOI: 10.1111/bjd.15068
14. Williams J, Brasch H, Bockett N, Patel J, Paterson E, Davis P, Tan S. Embryonic Stem Cell-like Population in Hypertrophic Port-wine Stain. *Journal of Vascular Anomalies*. 2021;2. doi: 10.1097/JOVA.0000000000000006
15. Shirley MD, Tang H, Gallione CJ, Baugher JD, Frelin LP, Cohen B, North PE, Marchuk DA, Comi AM, Pevsner J. Sturge-Weber Syndrome and Port-Wine Stains Caused by Somatic Mutation in GNAQ. *N Engl J Med*. 2013;368:1971-1979. doi: 10.1056/NEJMoa1213507

16. Lian CG, Sholl LM, Zakka LR, O TM, Liu C, Xu S, Stanek E, Garcia E, Jia Y, MacConaill LE, et al. Novel genetic mutations in a sporadic port-wine stain. *JAMA Dermatol*. 2014;150:1336-1340. doi: 10.1001/jamadermatol.2014.1244
17. Couto JA, Huang L, Vivero MP, Kamitaki N, Maclellan RA, Mulliken JB, Bischoff J, Warman ML, Greene AK. Endothelial Cells from Capillary Malformations Are Enriched for Somatic GNAQ Mutations. *Plast Reconstr Surg*. 2016;137:77e-82e. doi: 10.1097/PRS.0000000000001868
18. Huang L, Bichsel C, Norris AL, Thorpe J, Pevsner J, Alexandrescu S, Pinto A, Zurakowski D, Kleiman RJ, Sahin M, et al. Endothelial GNAQ p.R183Q Increases ANGPT2 (Angiopoietin-2) and Drives Formation of Enlarged Blood Vessels. *Arterioscler Thromb Vasc Biol*. 2022;42:e27-e43. doi: 10.1161/ATVBAHA.121.316651
19. Wetzel-Strong SE, Galeffi F, Benavides C, Patrucco M, Bullock JL, Gallione CJ, Lee HK, Marchuk DA. Developmental expression of the Sturge-Weber syndrome-associated genetic mutation in Gnaq: a formal test of Happle's paradominant inheritance hypothesis. *Genetics*. 2023;224. doi: 10.1093/genetics/iyad077
20. Nguyen V, Gao C, Hochman ML, Kravitz J, Chen EH, Friedman HI, Wenceslau CF, Chen D, Wang Y, Nelson JS, et al. Endothelial cells differentiated from patient dermal fibroblast-derived induced pluripotent stem cells resemble vascular malformations of Port Wine Birthmark. *Br J Dermatol*. 2023. doi: 10.1093/bjd/ljad330
21. Nguyen V, Gao C, Hochman ML, Kravitz J, Chen EH, Friedman HI, Wenceslau CF, Chen D, Wang Y, Nelson JS, et al. Supporting materials: Endothelial cells differentiated from patient dermal fibroblast-derived induced pluripotent stem cells resemble vascular malformations of Port Wine Birthmark. *bioRxiv*. 2023. doi: 10.1101/2023.07.02.547408
22. Nasim S, Bichsel C, Dayneka S, Mannix R, Holm A, Vivero M, Alexandrescu S, Pinto A, Greene AK, Ingber DE, et al. MRC1 and LYVE1 expressing macrophages in vascular beds of GNAQ p.R183Q driven capillary malformations in Sturge Weber syndrome. *Acta Neuropathol Commun*. 2024;12:47. doi: 10.1186/s40478-024-01757-4
23. Nasim S, Bichsel C, Pinto A, Alexandrescu S, Kozakewich H, Bischoff J. Similarities and differences between brain and skin GNAQ p.R183Q driven capillary malformations. *Angiogenesis*. 2024;27:931-941. doi: 10.1007/s10456-024-09950-8
24. Tan W, Chernova M, Gao L, Sun V, Liu H, Jia W, Langer S, Wang G, Mihm MC, Jr., Nelson JS. Sustained activation of c-Jun N-terminal and extracellular signal-regulated kinases in port-wine stain blood vessels. *J Am Acad Dermatol*. 2014;71:964-968. doi: 10.1016/j.jaad.2014.07.025
25. Love MI, Huber W, Anders S. Moderated estimation of fold change and dispersion for RNA-seq data with DESeq2. *Genome Biol*. 2014;15:550. doi: 10.1186/s13059-014-0550-8
26. Subramanian A, Tamayo P, Mootha VK, Mukherjee S, Ebert BL, Gillette MA, Paulovich A, Pomeroy SL, Golub TR, Lander ES, et al. Gene set enrichment analysis: a knowledge-based approach for interpreting genome-wide expression profiles. *Proc Natl Acad Sci U S A*. 2005;102:15545-15550. doi: 10.1073/pnas.0506580102
27. Rufaihah AJ, Huang NF, Kim J, Herold J, Volz KS, Park TS, Lee JC, Zambidis ET, Reijo-Pera R, Cooke JP. Human induced pluripotent stem cell-derived endothelial cells exhibit functional heterogeneity. *Am J Transl Res*. 2013;5:21-35.
28. Ikuno T, Masumoto H, Yamamizu K, Yoshioka M, Minakata K, Ikeda T, Sakata R, Yamashita JK. Efficient and robust differentiation of endothelial cells from human induced pluripotent stem cells via lineage control with VEGF and cyclic AMP. *PLoS One*. 2017;12:e0173271. doi: 10.1371/journal.pone.0173271
29. Williams IM, Wu JC. Generation of Endothelial Cells From Human Pluripotent Stem Cells. *Arterioscler Thromb Vasc Biol*. 2019;39:1317-1329. doi: 10.1161/ATVBAHA.119.312265

30. Patsch C, Challet-Meylan L, Thoma EC, Urich E, Heckel T, O'Sullivan JF, Grainger SJ, Kapp FG, Sun L, Christensen K, et al. Generation of vascular endothelial and smooth muscle cells from human pluripotent stem cells. *Nat Cell Biol*. 2015;17:994-1003. doi: 10.1038/ncb3205
31. Pierson Smela MD, Kramme CC, Fortuna PRJ, Adams JL, Su R, Dong E, Kobayashi M, Brixi G, Kavirayuni VS, Tysinger E, et al. Directed differentiation of human iPSCs to functional ovarian granulosa-like cells via transcription factor overexpression. *Elife*. 2023;12. doi: 10.7554/eLife.83291
32. Langmead B, Salzberg SL. Fast gapped-read alignment with Bowtie 2. *Nat Methods*. 2012;9:357-359. doi: 10.1038/nmeth.1923
33. Zhang Y, Liu T, Meyer CA, Eeckhoute J, Johnson DS, Bernstein BE, Nusbaum C, Myers RM, Brown M, Li W, et al. Model-based analysis of ChIP-Seq (MACS). *Genome Biol*. 2008;9:R137. doi: 10.1186/gb-2008-9-9-r137
34. Galaxy C. The Galaxy platform for accessible, reproducible, and collaborative data analyses: 2024 update. *Nucleic Acids Res*. 2024;52:W83-W94. doi: 10.1093/nar/gkae410
35. Kamimoto K, Stringa B, Hoffmann CM, Jindal K, Solnica-Krezel L, Morris SA. Dissecting cell identity via network inference and in silico gene perturbation. *Nature*. 2023;614:742-751. doi: 10.1038/s41586-022-05688-9
36. Sissaoui S, Yu J, Yan A, Li R, Yukselen O, Kucukural A, Zhu LJ, Lawson ND. Genomic Characterization of Endothelial Enhancers Reveals a Multifunctional Role for NR2F2 in Regulation of Arteriovenous Gene Expression. *Circ Res*. 2020;126:875-888. doi: 10.1161/CIRCRESAHA.119.316075
37. He Y, Tacconi C, Dieterich LC, Kim J, Restivo G, Gousopoulos E, Lindenblatt N, Levesque MP, Claassen M, Detmar M. Novel Blood Vascular Endothelial Subtype-Specific Markers in Human Skin Unearthed by Single-Cell Transcriptomic Profiling. *Cells*. 2022;11. doi: 10.3390/cells11071111
38. Chi JT, Chang HY, Haraldsen G, Jahnsen FL, Troyanskaya OG, Chang DS, Wang Z, Rockson SG, van de Rijn M, Botstein D, et al. Endothelial cell diversity revealed by global expression profiling. *Proc Natl Acad Sci U S A*. 2003;100:10623-10628. doi: 10.1073/pnas.1434429100
39. Rieker C, Migliavacca E, Vaucher A, Baud G, Marquis J, Charpagne A, Hegde N, Guignard L, McLachlan M, Pooler AM. Apolipoprotein E4 Expression Causes Gain of Toxic Function in Isogenic Human Induced Pluripotent Stem Cell-Derived Endothelial Cells. *Arterioscler Thromb Vasc Biol*. 2019;39:e195-e207. doi: 10.1161/ATVBAHA.118.312261
40. Li W, Mukouyama YS. Tissue-specific venous expression of the EPH family receptor EphB1 in the skin vasculature. *Dev Dyn*. 2013;242:976-988. doi: 10.1002/dvdy.23985
41. Perera P, Kurban AK, Ryan TJ. The development of the cutaneous microvascular system in the newborn. *Br J Dermtol* 1970;82:86-91.
42. Gao L, Yin R, Wang H, Guo W, Song W, Nelson JS, Tan W, Wang G. Ultrastructural Characterization of Hyperactive Endothelial Cells, Pericytes and Fibroblasts in Hypertrophic and Nodular Port Wine Stain Lesions. *Br J Dermatol*. 2017;177:e105-e108. doi: 10.1111/bjd.15373
43. Mori M, Sakamoto A, Kawakami R, Guo L, Slenders L, Mosquera JV, Ghosh SKB, Wesseling M, Shiraki T, Bellissard A, et al. CD163(+) Macrophages Induce Endothelial-to-Mesenchymal Transition in Atheroma. *Circ Res*. 2024;135:e4-e23. doi: 10.1161/CIRCRESAHA.123.324082
44. Gui Z, Zhang X, Han Q, Hang Z, Tan R, Gu M, Wang Z. Macrophage polarization induces endothelium-to-myofibroblast transition in chronic allograft dysfunction. *Ren Fail*. 2023;45:2220418. doi: 10.1080/0886022X.2023.2220418
45. Romano E, Rosa I, Fioretto BS, Manetti M. The contribution of endothelial cells to tissue fibrosis. *Curr Opin Rheumatol*. 2024;36:52-60. doi: 10.1097/BOR.0000000000000963

46. Manetti M, Romano E, Rosa I, Guiducci S, Bellando-Randone S, De Paulis A, Ibba-Manneschi L, Matucci-Cerinic M. Endothelial-to-mesenchymal transition contributes to endothelial dysfunction and dermal fibrosis in systemic sclerosis. *Ann Rheum Dis*. 2017;76:924-934. doi: 10.1136/annrheumdis-2016-210229
47. Wu SP, Kao CY, Wang L, Creighton CJ, Yang J, Donti TR, Harmancey R, Vasquez HG, Graham BH, Bellen HJ, et al. Increased COUP-TFII expression in adult hearts induces mitochondrial dysfunction resulting in heart failure. *Nat Commun*. 2015;6:8245. doi: 10.1038/ncomms9245
48. Zhou B, Jia L, Zhang Z, Xiang L, Yuan Y, Zheng P, Liu B, Ren X, Bian H, Xie L, et al. The Nuclear Orphan Receptor NR2F6 Promotes Hepatic Steatosis through Upregulation of Fatty Acid Transporter CD36. *Adv Sci (Weinh)*. 2020;7:2002273. doi: 10.1002/advs.202002273
49. Xia B, Hou L, Kang H, Chang W, Liu Y, Zhang Y, Ding Y. NR2F2 plays a major role in insulin-induced epithelial-mesenchymal transition in breast cancer cells. *BMC Cancer*. 2020;20:626. doi: 10.1186/s12885-020-07107-6